

# Dynamic model of CHO cell metabolism

Ryan P. Nolan<sup>a,b</sup>, Kyongbum Lee<sup>b,\*</sup>

<sup>a</sup> Pfizer, Culture Process Development, 1 Burtt Road, Andover, MA 01810, USA

<sup>b</sup> Department of Chemical and Biological Engineering, Tufts University, 4 Colby Street, Medford, MA 02155, USA

## ARTICLE INFO

### Article history:

Received 7 September 2010

Received in revised form

28 September 2010

Accepted 29 September 2010

Available online 7 October 2010

### Keywords:

Dynamic simulation

Fed-batch

Metabolic shift

Lactate metabolism

Redox metabolism

## ABSTRACT

Fed-batch cultures are extensively used for the production of therapeutic proteins. However, process optimization is hampered by lack of quantitative models of mammalian cellular metabolism in these cultures. This paper presents a new kinetic model of CHO cell metabolism and a novel framework for simulating the dynamics of metabolic and biosynthetic pathways of these cells grown in fed-batch culture. The model defines a subset of the intracellular reactions with kinetic rate expressions based on extracellular metabolite concentrations and temperature- and redox-dependent regulatory variables. The simulation uses the rate expressions to calculate pseudo-steady state flux distributions and extracellular metabolite concentrations at discrete time points. Experimental data collected in this study for several different CHO cell fed-batch cultures are used to derive the rate expressions, fit the parameters, and validate the model. The simulations accurately predicted the effects of process variables, including temperature shift, seed density, specific productivity, and nutrient concentrations.

© 2010 Elsevier Inc. All rights reserved.

## 1. Introduction

Biologics have emerged as successful treatments for numerous diseases, including diabetes, arthritis, multiple sclerosis, cancer, anemia, and HIV. In 2008, revenue generated from each of the top 10 biologics ranged \$3–6 billion (Harris, 2009). By 2015, biologics are expected to account for > 50% of all new product approvals (Harris, 2009).

Most recombinant therapeutic proteins are produced in eukaryotic cells to enable post-translational modifications. Chinese hamster ovary (CHO) cells have become the standard industry host, owing to well-characterized technologies for gene transfection, amplification, and clone selection (Butler, 2005). CHO cells are commonly grown in a fed-batch culture, as such processes afford ease of operation and scale-up, and provide a higher volumetric productivity compared to batch re-feed and perfusion cultures.

Even though fed-batch bioprocesses have been used for decades, important cellular metabolic events remain poorly understood. This is especially true with respect to the mechanisms driving the “metabolic shift” characterized by a reversal in lactate and ammonia production following a reduction in reactor temperature (Ma et al., 2009). Throughout the duration of a fed-batch, numerous process perturbations occur, including temperature change and fluctuations in nutrient and inhibitor concentrations. Changes in the seed density or time of

temperature shift also has a dramatic effect on cell culture performance. Even when using rational methods for media formulation (Luan et al., 2007), nutrients are often at sub-optimal concentrations due to their utilization in unaccounted metabolic pathways. As a result, process optimization generally relies on statistical design of experiments (DOE) and/or high-throughput screening (HTS) methods, which provide limited mechanistic insights (Legmann et al., 2009).

Mathematical models of metabolism have been applied extensively in biotechnology, typically with the goal of optimizing the production efficiency of a cell and/or process. Metabolic flux analysis (MFA) and flux balance analysis (FBA) are widely used to characterize the state of cellular metabolism (Boghigian et al., 2010; Goudar et al., 2010; Quek et al., 2010). These analyses are based on pseudo-steady state mass balances around intracellular metabolites. Combined with measurements on extracellular metabolite uptake and output rates, a comprehensive estimate can be obtained for the intracellular metabolic flux distribution. In the case of FBA, assumptions about optimality and a metabolic objective, such as biomass formation, are introduced to solve underdetermined problems. Providing a snapshot in time, MFA and FBA models can be used to calculate the redistribution of fluxes when cells are exposed to variations in environmental conditions. Mechanistic insights into specific metabolic events may also be inferred. However, steady state models cannot account for concentration dependencies, and thus are limited in their ability to predict dynamic cellular responses to external medium changes and other perturbations.

One way to achieve dynamic predictions is to define algebraic expressions for the reaction rates as functions of metabolite

\* Corresponding author. Fax: +1 617 627 3991.

E-mail address: [kyongbum.lee@tufts.edu](mailto:kyongbum.lee@tufts.edu) (K. Lee).

concentrations. However, such expressions include a large number of parameters, generally limiting model coverage to select pathways or sub-networks and short time scales (Chassagnole et al., 2002). Recently, hybrid models have been introduced that attempt to simulate whole-cell metabolic dynamics by combining steady state flux analysis and kinetic rate expressions. Often referred to as dynamic flux balance analysis (dFBA) models (Mahadevan et al., 2002), these models represent uptake and/or output reactions using kinetic rate expressions, thereby accommodating time and concentration dependencies. Intracellular reactions are calculated from metabolite balances by assuming pseudo-steady state, which significantly reduces the total number of kinetic parameters that need to be estimated. A typical simulation divides the culture into small time steps, and assuming the existence of a pseudo-steady state at each step, the dynamic metabolic changes of a culture can be simulated.

However, modeling whole-cell metabolism is still extremely challenging. It is often difficult to model all extracellular reactions with concentration-dependent rate equations and maintain sufficient constraints for flux calculations. Consequently, dFBA models require one or more of the following simplifying assumptions: reducing the network size, through the use of macroscopic reactions (Gao et al., 2007; Mahadevan et al., 2002; Provost et al., 2006) or a small metabolite sub-set (Gao et al., 2007; Hjersted and Henson, 2006; Mahadevan et al., 2002; Provost et al., 2006; Sainz et al., 2003); using a universal cellular objective function, for example, maximizing biomass (Mahadevan et al., 2002; Oddone et al., 2009); nesting objective functions, for example, to accommodate recombinant protein production (Oddone et al., 2009) or energy utilization (Meadows et al., 2009); adding constraints, such as pre-defined reaction rates (Meadows et al., 2009) or empirical equations; reducing time scales, for example, modeling only a small timeframe (of order hours) (Hjersted and Henson, 2006; Mahadevan et al., 2002; Meadows et al., 2009; Oddone et al., 2009); and/or dividing the process into distinct phases, with defined functions to transition between phases (Gao et al., 2007; Provost et al., 2006).

Depending on the goal, the aforementioned assumptions may be applicable to some cell culture systems; however, for the purpose of modeling an industry relevant mammalian fed-batch culture, many of these simplifications are not appropriate. From the perspective of a process engineer, an ideal model should: (1) use as a set of inputs only initial metabolite concentrations and cell density, and a fixed set of parameters; (2) have kinetic expressions be dependent on metabolite concentrations, cell density, and process parameters only; (3) have a mechanistic foundation such that the resulting dynamics can be traced back to biochemical pathways; (4) be comprehensive, including all major carbon and energy metabolic pathways; (5) determine how manipulations in process variables will impact cell growth and product (e.g. antibody) formation (via feed forward and feedback regulation); and (6) be capable of modeling the long-term dynamics of a fed-batch (on the order of days to weeks).

In this work, a novel simulation framework is presented which builds on the dFBA structure to predict the metabolic dynamics of CHO cells in fed-batch culture. This framework defines rate expressions for cytosolic reactions based on extracellular metabolite concentrations, enabling direct calculation of measurable variables. Additionally, the model accounts for coordinated regulation of the various pathways by incorporating temperature- and redox-dependent variables. Reaction rate expressions and model parameters are derived from CHO cell fed-batch data obtained in this study. Application of the model to process improvement is illustrated by comparing the predicted and observed responses to various changes in process parameters.

## 2. Materials and methods

### 2.1. Cell culture

For fed-batch cultures, CHO-K1 cells producing a recombinant monoclonal antibody (obtained from Pfizer, formally Wyeth BioPharma) were seeded at a density of  $1.5 \times 10^6$  cells/mL in 10% conditioned medium and 90% fresh proprietary medium. A 2-L Applikon bioreactor controlled pH at 7.0, temperature at 37 °C, and dissolved oxygen at 30%. Agitation and aeration were controlled with a rushton impeller at 200 rpm and a 15 µm sintered steel sparger. At day 3, the temperature was reduced to 31 °C. Starting on day 3 daily bolus feeds at 3% v/v of a proprietary media feed were supplied for the remainder of the culture. Samples were taken daily for analysis.

### 2.2. Metabolite analysis

Daily samples were analyzed for viable cell density (Cedex, Roche Innovatis AG, Germany), glucose, lactate, ammonia (Nova 400 Bioanalyzer, Nova Biomedical, Waltham, MA), and osmolarity (Advanced Model 3900 Multi-Sample Osmometer, Advanced Instruments, Norwood, MA). Additional samples were centrifuged and the supernatant frozen for the following assays. Amino acids were analyzed using a UPLC (Waters AcQuity UPLC, Waters, Milford, MA), lactate dehydrogenase (LDH) using a standard assay kit (CytoTox 96 Cytotoxicity Assay, Promega, Madison, WI), and antibody titer using protein A affinity chromatography (Applied Biosystems, Foster City, CA). Dead cell density was determined from the amount of LDH released into the media from lysed cells. Total cell density was calculated as the sum of the viable and dead cell densities. Viability was calculated as the fraction of viable cells over total cells. Biomass composition was estimated to be 2% RNA, 1% DNA, 4% carbohydrate, 91% protein, and 2% lipid, mol/mol (Bonarius et al., 1996; Sheikh et al., 2005). RNA composition was estimated to be 18% ATP, 34% GTP, 18% UTP, and 30% CTP, mol/mol (Sheikh et al., 2005). DNA composition was estimated to be 30% dATP, 20% dGTP, 30% dTTP, and 20% dCTP, mol/mol (Sheikh et al., 2005). Lipid composition was estimated to be 26% cholesterol, 59% phospholipid, and 15% sphingolipid, mol/mol (Zupke and Stephanopoulos, 1995). The molecular weight of biomass was calculated by summing the product of the molar percentages and respective molecular weights of each biomass constituent (e.g. biomass = 2% RNA  $\times$  501 g/mol + 1% DNA  $\times$  487 g/mol + 4% carbohydrate  $\times$  180 g/mol + 91% protein  $\times$  127 g/mol + 2% lipid  $\times$  662 g/mol = 151 g/mol). The constituent molecular weights were calculated in an analogous manner (e.g. RNA = 18% ATP  $\times$  507 g/mol + 34% GTP  $\times$  523 g/mol + 18% UTP  $\times$  484 g/mol + 30% CTP  $\times$  483 g/mol = 501 g/mol). Alternatively, the elemental composition of each biomass constituent can be used to derive the elemental formula of biomass. The result was  $C_{5.68}N_{1.40}O_{2.92}H_{11.49}S_{0.04}P_{0.09}$ . Both approaches yielded the same molecular weight of 151 g/mol. Similarly, for antibody, a molecular weight of 126 g/mol was calculated based on the weighted average of the molecular weights of the component amino acids and the elemental formula determined to be  $C_{4.81}N_{1.28}O_{2.51}H_{9.44}S_{0.03}$ . Based on the measured dry cell weight of 350 pg/cell, it was determined that  $1 \times 10^6$  cells/mL is equivalent to 2.31 mM biomass. It was determined that 1 g/L antibody is equivalent to 7.94 mM antibody. Oxygen uptake rate (OUR) was measured daily by sparging the culture to 70% dissolved oxygen, turning off the sparge, recording the drop in dissolved oxygen over time, and then normalizing to the viable cell density. It was previously determined (data not shown) that oxygen loss through the headspace was negligible.

### 2.3. Network formulation

Details behind the formulation and reduction of the network model have previously been described (Nolan and Lee, 2009). Briefly, a network of reactions collected from the KEGG database (for the hamster analog mouse) was used as a starting point. This network consisted of approximately 200 reactions and 200 metabolites, comprising the metabolic pathways of glycolysis, pentose phosphate pathway (PPP), citrate cycle, amino acid metabolism, oxidative phosphorylation, and biomass synthesis. Biomass synthesis was related to nucleotide, carbohydrate, protein, and lipid synthesis. Antibody synthesis was defined to include the standard reactions of mammalian cell protein translation, but with amino acid stoichiometry specified by the antibody sequence. The model reduction strategy was as follows. All linear pathways were collapsed to external carbon metabolites and intracellular carbon and currency metabolites (e.g. NADH, NADPH, FADH<sub>2</sub>, ATP, etc.) of the TCA cycle. Especial care was taken to preserve all stoichiometric relationships while collapsing reactions and removing intermediates. For example, the condensed model did not explicitly include NADPH and ribose-5-phosphate, because the reaction pathways producing (PPP) and consuming (lipid and nucleotide synthesis) these metabolites were lumped into the final biomass equation. As a final step, a

reaction relating the antiport of cystine and glutamate was added, as this exchange significantly impacts the redox state of mammalian cells (Sato et al., 2005).

The final network model, which is a reduced and simplified form of the original network, consisted of 24 metabolites and 34 reactions. The model composition is similar to several of the previously published mammalian cellular networks (Altamirano et al., 2001; Bonarius et al., 1996). The rank and condition number of the full stoichiometric matrix are 24 and 33, respectively. The degree of freedom is zero.

A schematic representation of the network is depicted in Fig. 1. The reactions are listed in Table 1. The model was compartmentalized into the cytosol and mitochondria only for an NADH transport. Transport of NADH into the mitochondria was assumed to occur equally through the malate–aspartate shuttle and the glycerol 3-phosphate shuttle. It should be noted that an NADH was the only metabolite compartmentalized into cytosolic and mitochondrial pools.

### 2.4. Network stoichiometry

Based on stoichiometry, the ATP requirements for producing 1 mol of biomass and 1 mol of antibody are 3.78 and 4 mol, respectively. A mass balance on ATP indicated that the production

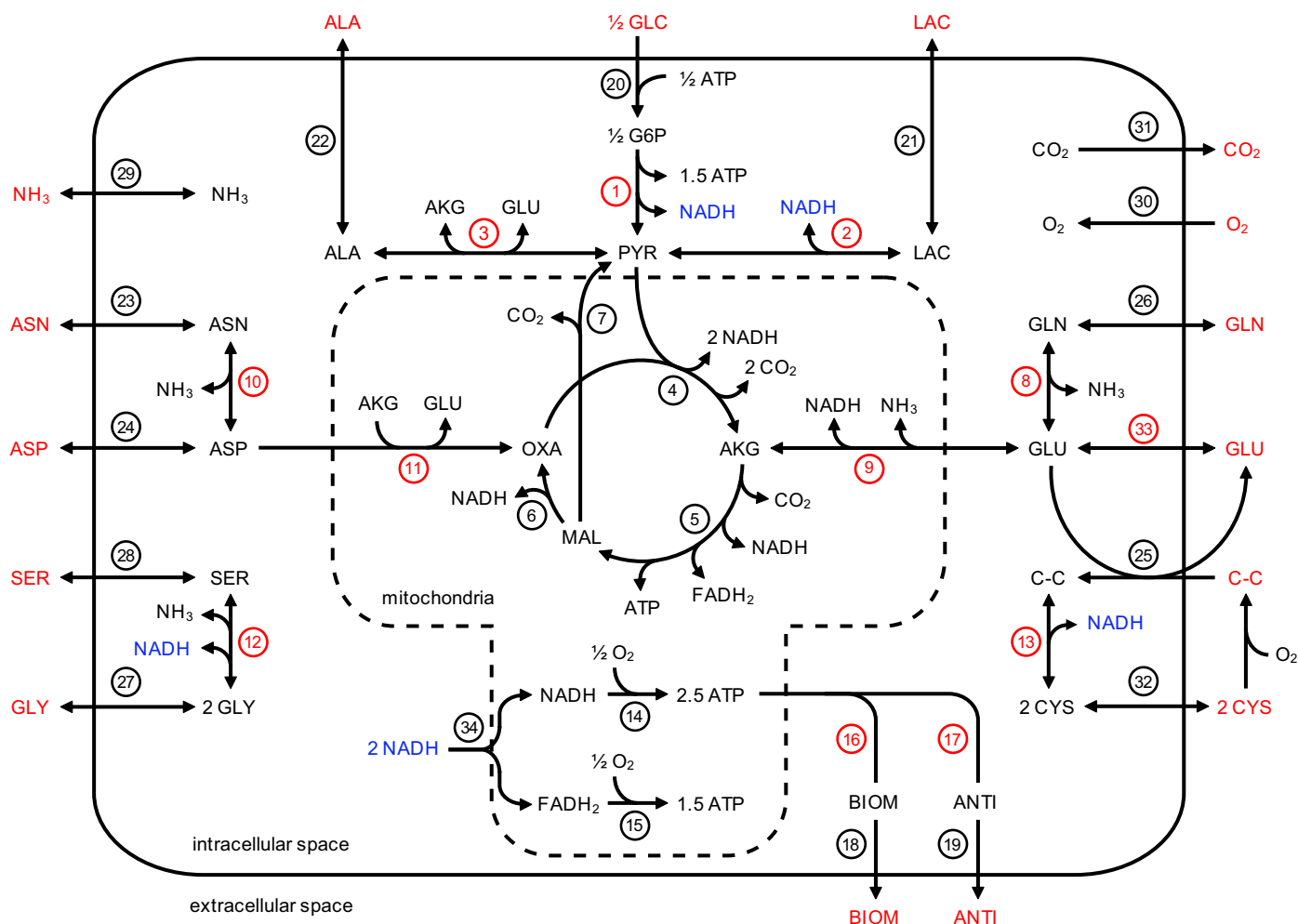


**Fig. 1.** Schematic representation of the CHO metabolic reaction network. Metabolites are distinguished by extracellular (red) and intracellular (black). NADH is distinguished by cytosolic (blue) and mitochondrial (black). Reactions in red are those for which kinetic rate expressions are defined in the dynamic simulation. (For interpretation of the references to colour in this figure legend, the reader is referred to the web version of this article.)

**Table 1**  
Reactions used for flux analysis.

Reaction	Stoichiometry
1	G6P → 2 PYR + 3 ATP + 2 <b>NADH</b>
2	PYR + <b>NADH</b> ↔ LAC
3	PYR + GLU ↔ ALA + AKG
4	PYR + OXA → AKG + 2 CO <sub>2</sub> + 2 NADH
5	AKG → MAL + CO <sub>2</sub> + NADH + FADH <sub>2</sub> + ATP
6	MAL → OXA + NADH
7	MAL → PYR + CO <sub>2</sub>
8	GLN ↔ GLU + NH <sub>3</sub>
9	AKG + NH <sub>3</sub> + NADH ↔ GLU
10	ASN ↔ ASP + NH <sub>3</sub>
11	ASP + AKG → OXA + GLU
12	SER + CO <sub>2</sub> + NH <sub>3</sub> + <b>NADH</b> ↔ 2 GLY
13	C-C + <b>NADH</b> → 2 CYS
14	NADH + 0.5 O <sub>2</sub> → 2.5 ATP
15	FADH <sub>2</sub> + 0.5 O <sub>2</sub> → 1.5 ATP
16	0.084 ALA + 0.041 ASN + 0.080 ASP + 8.680 ATP + 0.026 CYS + 0.452 G6P + 0.087 GLN + 0.056 GLY + 0.427 OXA + 0.096 SER → BIOM + 0.004 FADH <sub>2</sub> + 0.008 GLU + 0.445 MAL + 0.639 NADH + 0.209 PYR
17	0.061 ALA + 0.034 ASN + 0.039 ASP + 9.200 ATP + 0.024 CYS + 0.048 GLU + 0.045 GLN + 0.072 GLY + 0.126 SER → ANTI
18	BIOM → <b>BIOM</b>
19	ANTI → <b>ANTI</b>
20	<b>GLC</b> + ATP → G6P
21	LAC ↔ <b>LAC</b>
22	ALA ↔ <b>ALA</b>
23	<b>ASN</b> → ASN
24	ASP ↔ <b>ASP</b>
25	<b>C-C</b> + GLU → C-C + <b>GLU</b>
26	<b>GLN</b> ↔ GLN
27	GLY ↔ <b>GLY</b>
28	<b>SER</b> → SER
29	NH <sub>3</sub> ↔ <b>NH<sub>3</sub></b>
30	<b>O<sub>2</sub></b> → O <sub>2</sub>
31	CO <sub>2</sub> → <b>CO<sub>2</sub></b>
32	2 CYS + O <sub>2</sub> → C-C
33	GLU → <b>GLU</b>
34	<b>NADH</b> → 0.5 NADH + 0.5 FADH <sub>2</sub>

Metabolites are distinguished by extracellular (red) and intracellular (black). NADH is distinguished by cytosolic (blue) and mitochondrial (black).

from glycolysis (glucose uptake minus biomass and pentose phosphate pathway utilization) and oxidative phosphorylation (assuming 2 mol ATP produced per 0.5 mol oxygen consumed minus the oxygen consumed for biomass) exceeded the consumption for biomass and antibody synthesis (the major ATP consuming reactions) by a factor of 2.3. This difference remained nearly constant for the duration of a fed-batch culture maintained at 37 °C. The excess ATP was attributed to maintenance-related processes, such as membrane transport and protein folding and excretion. Therefore, the ATP requirements for 1 mol of biomass and 1 mol of antibody were set to 8.68 and 9.2 mol, respectively. According to experimental data obtained in this study, at 31 °C the amount of ATP produced from oxidative phosphorylation was two-fold greater than an ATP consumption. This discrepancy could be explained by increased proton leakage in the mitochondria. The stoichiometry for oxidative phosphorylation was tied to temperature, such that for every one NADH or FADH<sub>2</sub> oxidized at

37 °C, 2.5 NADH or FADH<sub>2</sub> are required to produce the equivalent amount of ATP at 31 °C.

## 2.5. Flux definition

Fluxes for each metabolite were calculated according to the following formula:

$$v_{t_{avg}} = \frac{(C_{t_B} - C_{t_A}) 1000}{(t_B - t_A) VCD_{avg}} \quad (1)$$

where  $t_A$  and  $t_B$  are consecutive time points (units of days) such that  $t_A < t_B$ ,  $t_{avg}$  and  $VCD_{avg}$  are the average time and average viable cell density (units of 10<sup>6</sup> cells/mL), respectively, over  $t_A$  and  $t_B$ , and  $C_t$  is the metabolite concentration (units of mM) at time  $t$ . The units of flux,  $v$ , are nmol/10<sup>6</sup> cells/day. We have also evaluated other numerical differentiation methods, such as

differentiating polynomial functions fitted to discrete time data, and found that the results were equivalent to Eq. (1).

## 2.6. Metabolic flux analysis

Calculation of the reaction flux distribution,  $\mathbf{v}$ , for MFA was performed by solving the following optimization problem:

$$\begin{aligned} \text{Minimize : } & \sum \left( \frac{v_k^{\text{calc}} - v_k^{\text{meas}}}{v_k^{\text{meas}}} \right)^2 \forall k \in \{\text{measured fluxes}\} \\ \text{Subject to : } & \mathbf{S} \cdot \mathbf{v} = \mathbf{0} \\ & \mathbf{0} < \mathbf{v}_{\text{irrev}} \end{aligned} \quad (2)$$

where  $\mathbf{S}$  is the stoichiometric matrix,  $v_k^{\text{calc}}$  and  $v_k^{\text{meas}}$  are, respectively, the calculated and measured flux components of  $\mathbf{v}$ , the reaction flux vector, and  $\mathbf{v}_{\text{irrev}}$  are the irreversible reactions in  $\mathbf{v}$ . Reversible reactions, i.e.  $\mathbf{v}_{\text{rev}}$ , have no flux bounds. For MFA where measurements on extracellular metabolite exchange fluxes are available, the measured fluxes,  $k$ , are the set of experimentally determined exchange fluxes. For MFA used in *dynamic simulations*, where exchange fluxes are unknown, the measured fluxes refer to the intracellular reaction rates defined with kinetic expressions.

## 2.7. Kinetic rate expressions

One way to adapt MFA or FBA for unsteady systems has been to model the time evolution of the exchanges fluxes with kinetic rate expressions (Hjersted and Henson, 2006; Meadows et al., 2009). This approach assumes that the uptake rates are the dominant factors driving changes in the system. However, the  $K_m$  (Michaelis–Menten half-saturation constant) for most metabolite transporters is large relative to the extracellular concentration of the metabolites (Hundal et al., 1989), suggesting that the exchange of a metabolite is not controlled by the transporter, but rather the intracellular enzymes. While the intracellular metabolites are assumed to be at pseudo-steady state, the extracellular concentrations influence the effective intracellular concentrations. Therefore, the approach taken in this paper is to model many of the cytosolic intracellular enzyme-catalyzed reactions with kinetic rate expressions (Liebermeister and Klipp, 2006), where the concentration dependencies are based on the associated extracellular metabolite concentration. In this formulation, the uptake rate for a given metabolite is controlled by several intracellular reactions, rather than a single transporter. This formulation models the magnitude and direction of reversible enzymes based on the concentrations of the substrate and product metabolites. This is extremely beneficial, as the reversible enzymes are directly responsible for much of the culture dynamics. The reactions colored in red in Fig. 1 are those for which a rate expression was defined. The reactions and their associated expressions are listed in Table 2.

Only cytosolic reactions were defined with kinetic rate expressions, as these provided sufficient constraints for calculation of the remaining reaction rates via MFA. One exception was the exchange rate for glutamate. A kinetic expression for glutamate exchange was necessary to constrain the balance around this metabolite. The kinetic rate expressions were systematically defined for each reaction as follows. First, a convenience kinetic expression (Liebermeister and Klipp, 2006) was defined and compared to experimental rate data for three different CHO-K1 cell lines (high specific productivity, average specific productivity, and non-transfected) under slightly different fed-batch conditions (variations in seed densities and culture media concentrations). Second, an *initial* set of parameters were estimated based on experimental data collected in this study as well as data

found in the published literature. These initial parameters were subsequently refined using non-linear optimization with metabolite concentration time course data. If the traditional convenience kinetic expression did not fit the data for all three cell lines (using an  $R^2$  cutoff of 0.7), then additional regulatory factors were introduced based on biochemical knowledge. Temperature- and redox-dependent regulatory factors were defined as variables that scaled

**Table 2**  
Kinetic rate expressions.

Reaction	Kinetic expression	Parameters
1	$v_1 = \frac{v_{\max 1} \left( \frac{GLC}{K_{m1}} \right)}{\left( 1 + \left( \frac{LAC}{K_{i1}} \right) \exp_1 \right) \left( 1 + \frac{GLC}{K_{m1}} \right)}$	$v_{\max 1}$ , $K_{m1}$ , $K_{i1}$ , $TC_1$ , $\exp_1$
2	$v_2 = (R-1)v_{\max 2} \text{ for } R \geq 1$ $v_2 = \frac{(R-1)v_{\max 2} \left( \frac{LAC}{K_{m2}} \right)}{1 + \left( \frac{LAC}{K_{m2}} \right)} \text{ for } R < 1$	$v_{\max 2}$ , $K_{m2}$ , $R$
3	$v_3 = \frac{v_{\max 3f} \left( \frac{GLC}{K_{m3c}} \right) - v_{\max 3r} TC_{3b} \left( \frac{ALA}{K_{m3b}} \right)}{1 + \left( \frac{GLC}{K_{m3c}} \right) + \left( \frac{ALA}{K_{m3b}} \right)} \text{ for } R \geq 1$ $v_3 = \frac{v_{\max 3f} \left( \frac{LAC}{K_{m3a}} \right) - v_{\max 3r} \left( \frac{ALA}{K_{m3b}} \right)}{1 + \left( \frac{LAC}{K_{m3a}} \right) + \left( \frac{ALA}{K_{m3b}} \right)} \text{ for } R < 1$	$v_{\max 3f}$ , $v_{\max 3r}$ , $K_{m3a}$ , $K_{m3b}$ , $K_{m3c}$ , $TC_{3b}$ , $R$
8	$v_8 = \frac{v_{\max 8f} \left( \frac{GLN}{K_{m8a}} \right) - v_{\max 8r} \left( \frac{GLU}{K_{m8b}} \right) \left( \frac{NH_3}{K_{m8c}} \right)}{1 + \left( \frac{GLN}{K_{m8a}} \right) + \left( \frac{GLU}{K_{m8b}} \right) + \left( \frac{NH_3}{K_{m8c}} \right) + \left( \frac{GLU}{K_{m8b}} \right) \left( \frac{NH_3}{K_{m8c}} \right)}$	$v_{\max 8f}$ , $v_{\max 8r}$ , $K_{m8a}$ , $K_{m8b}$ , $K_{m8c}$
9	$v_9 = \frac{v_{\max 9f} v_3 \left( \frac{NH_3}{K_{m9}} \right) - v_{\max 9r} v_{11}}{1 + \left( \frac{NH_3}{K_{m9}} \right)}$	$v_{\max 9f}$ , $v_{\max 9r}$ , $K_{m9}$
10	$v_{10} = \frac{v_{\max 10f} \left( \frac{ASN}{K_{m10a}} \right) - v_{\max 10r} \left( \frac{ASP}{K_{m10b}} \right) \left( \frac{NH_3}{K_{m10c}} \right)}{1 + \left( \frac{ASN}{K_{m10a}} \right) + \left( \frac{ASP}{K_{m10b}} \right) + \left( \frac{NH_3}{K_{m10c}} \right) + \left( \frac{ASP}{K_{m10b}} \right) \left( \frac{NH_3}{K_{m10c}} \right)}$	$v_{\max 10f}$ , $v_{\max 10r}$ , $K_{m10a}$ , $K_{m10b}$ , $K_{m10c}$ , $TC_{10}$
11	$v_{11} = v_{\max 11} v_{10}$	$v_{\max 11}$
12	$v_{12} = \frac{v_{\max 12f} v_{16} \left( \frac{SER}{K_{m12a}} \right) - v_{\max 12r} \left( \frac{GLY}{K_{m12b}} \right)^2}{1 + \left( \frac{SER}{K_{m12a}} \right) + \left( \frac{GLY}{K_{m12b}} \right) + \left( \frac{GLY}{K_{m12b}} \right)^2}$	$v_{\max 12f}$ , $v_{\max 12r}$ , $K_{m12a}$ , $K_{m12b}$
13	$v_{13} = \frac{r v_{\max 13} \left( \frac{C-C}{K_{m13}} \right)}{1 + \left( \frac{C-C}{K_{m13}} \right)} \quad \begin{matrix} r = R, \text{ pretemp-shift} \\ r = 1, \text{ posttemp-shift} \end{matrix}$	$v_{\max 13}$ , $K_{m13}$ , $R$
16	$v_{16} = \frac{v_{\max 16} \left( \frac{GLN}{K_{m16a}} \right) \left( \frac{ASN}{K_{m16b}} \right)}{1 + \left( \frac{GLN}{K_{m16a}} \right) + \left( \frac{ASN}{K_{m16b}} \right) + \left( \frac{GLN}{K_{m16a}} \right) \left( \frac{ASN}{K_{m16b}} \right)} \text{ pre temp-shift}$ $v_{16} = \frac{v_{\max 16} \left( \frac{ASN}{K_{m16b}} \right) \left( \frac{GLC}{K_{m16c}} \right)}{1 + \left( \frac{ASN}{K_{m16b}} \right) + \left( \frac{GLC}{K_{m16c}} \right) + \left( \frac{ASN}{K_{m16b}} \right) \left( \frac{GLC}{K_{m16c}} \right)} \text{ post temp-shift}$	$v_{\max 16}$ , $K_{m16a}$ , $K_{m16b}$ , $TC_{16}$
17	$v_{17} = \frac{v_{\max 17}}{1 + \left( \frac{LAC}{K_{i17}} \right) \exp_{17}}$	$v_{\max 17}$ , $K_{i17}$ , $\exp_{17}$
33	$v_{33} = \frac{TC_{33} v_{\max 33} \left( \frac{GLN}{K_{m33a}} \right)}{1 + \left( \frac{GLN}{K_{m33a}} \right)} + 0.01 v_{16} - 0.05 v_{17}$	$v_{\max 33}$ , $K_{m33a}$ , $TC_{33}$

Standard convenience kinetic parameters used include maximum reaction velocity ( $v_{\max}$ ), half-saturation constant ( $K_m$ ), and inhibition constant ( $K_i$ ). New parameters include temperature-dependent constant ( $TC$ ) and redox variable ( $R$ ).



the  $\nu_{\max}$  parameter. Metabolite inhibition factors were defined in accordance with the convenience kinetic expression structure. Only known inhibitors, such as lactate and ammonia, were tested; ultimately, only lactate was used in the final set of equations. For most equations with extracellular metabolites as variables, definition of the rate expressions was straightforward. Equations involving intracellular metabolites required minor modifications. For example, in the lumped equation converting serine to glycine (Eq. (12) in Table 1),  $\text{CO}_2$  is involved as a co-reactant. Based on the steady state flux analysis, the majority of  $\text{CO}_2$  is produced from the biomass equation. Therefore, the biomass flux was incorporated as a  $\nu_{\max}$  scaling factor in this equation.

The antibody production rate depends on a number of factors, including the level of the recombinant gene expressed by the host cell. The gene expression level, which depends on the promoter strength and a host of other factors, will in turn influence the rate of translation, and thus the effective  $\nu_{\max}$ , albeit not necessarily in a linear fashion. In addition to the gene expression level, the antibody production rate also depends on the availability of amino acid substrates, cofactors, inhibitor metabolites, and temperature. It is assumed in this model that the effective  $K_m$  values of the amino acid substrates for antibody synthesis are low relative to their intracellular concentrations. Therefore, the amino acid substrates do not exert a dominant effect. Based on experimental data collected in this study, it is also assumed that the major inhibitor is lactate. Finally, temperature is expected to affect the antibody production rate through the  $\nu_{\max}$  parameter by influencing the intrinsic catalytic activities of the transcription and translation enzymes. The rationale and assumptions for all rate expressions are summarized in Table 3.

## 2.8. Redox metabolism

The effect of redox, i.e. the ratio of NADH to  $\text{NAD}^+$ , can have a significant effect on many reaction rates. However, the concentrations of these intracellular metabolites are relatively small (on

the order of  $\mu\text{M}$ , compared to mM for all other metabolites) and difficult to quantify accurately. It is thus difficult to exactly determine their contributions in kinetic rate expressions. Consequently, many kinetic models neglect the effect of these metabolites (Gao et al., 2007; Hjersted and Henson, 2006; Provost et al., 2006; Sainz et al., 2003). However, biochemical considerations suggest that the redox ratio be included as an essential control variable.

In modeling the availability of NADH, the first step is to compartmentalize the cofactor pool into cytosolic and mitochondrial components. The second step is to account for major sources and sinks of NADH. The sources include the TCA cycle in the mitochondria and glycolysis in the cytosol. The sinks include oxidative phosphorylation in the mitochondria, and under certain metabolic states, lactate dehydrogenase in the cytosol. MFA calculations showed that the amount of NADH produced within the mitochondria is not sufficient to meet the overall demand, resulting in a significant flow of NADH from the cytosol to the mitochondria via the glycerol 3-phosphate and malate-aspartate shuttles (Fig. 2). If NADH metabolism were perfectly balanced, nearly all of the NADH produced in the cytosol would be transported into the mitochondria and oxidized, resulting in a minimal overflow available for LDH. However, the rapid uptake of glucose by CHO cells results in an overproduction of NADH in the cytosol. The supply of NADH from the cytosol remains sufficient until the rate of glucose uptake decreases, either as a result of a reduction in glucose concentration or a reduction in temperature, or the demand from within the mitochondria increases, either from a higher growth rate or increased recombinant protein synthesis rate. When the NADH supply becomes insufficient, the lactate concentration is typically high, and combined with a low redox, leads to the reversal of LDH and consumption of lactate and production of NADH.

## 2.9. Redox variable

The redox variable,  $R$ , is defined as the rate of NADH generated in the cytosol (from glycolysis and biomass synthesis)

**Table 3**  
Rationale behind kinetic rate expressions.

Reaction	Description
1	The rate is dependent on extracellular GLC and inhibited by an extracellular LAC. The inhibition exponential factor is temperature-dependent. $\nu_{\max}$ is modified by a temperature-dependent constant.
2	The rates of LAC production and consumption are dependent on the redox state of the cell. Additionally, the LAC consumption rate is concentration-dependent.
3	Since intracellular PYR is at pseudo-steady state, the forward rate is governed by the corresponding extracellular metabolites producing PYR, i.e. extracellular GLC when $R \geq 1$ and extracellular LAC when $R < 1$ . The $\nu_{\max}$ 's are modified by a temperature-dependent constant to accommodate when $R > 1$ and LAC is produced during the late stage of the culture. The reverse rate is always dependent on an extracellular ALA. The $\nu_{\max}$ of the reverse rate is less sensitive to the temperature shift than the $\nu_{\max}$ of the forward rate. Since AKG and intracellular GLU are at pseudo-steady state, their contributions are considered insignificant.
8	The forward and reverse rates are concentration-dependent. $\nu_{\max}$ of the forward rate is modified by a temperature-dependent constant.
9	The forward rate is dependent on extracellular $\text{NH}_3$ and AKG. The contribution of AKG is from Reaction 3. The reverse rate is dependent on an intracellular GLU, produced from Reaction 11. The contribution of NADH is considered insignificant for this mitochondrial reaction.
10	The forward and reverse rates are concentration-dependent. $\nu_{\max}$ of the forward and reverse rates are modified by the same temperature-dependent constant.
11	The rate is dependent on an intracellular ASP, produced from Reaction 10. Since AKG and intracellular GLU are at pseudo-steady state, their contributions are considered insignificant.
12	The forward rate is dependent on extracellular SER and $\text{CO}_2$ . The contribution of $\text{CO}_2$ is predominantly from biomass synthesis, Reaction 16. The reverse rate is dependent on GLY. The contributions of $\text{NH}_3$ and NADH are considered insignificant compared to the other metabolites.
13	The rate is concentration-dependent. Cytosolic NADH affects the rate during the exponential growth phase when there is excess NADH in the cytosol, and is modeled by scaling $\nu_{\max}$ by $R$ .
16	The production of BIOM is dependent on GLN, ASN, and GLC. $\nu_{\max}$ is modified by a temperature-dependent constant. Initially, during the exponential growth phase when GLN is consumed, GLN and ASN control the growth rate, while the effect of GLC is negligible. Post-temperature shift when GLN is produced, it does not influence the growth rate, while ASN and GLC dominate. This is analogous to a diauxic shift.
17	The $\nu_{\max}$ of an ANTI production is intrinsic to each cell line; however, it is inhibited by the extracellular LAC concentration and a reduction in temperature. The inhibition exponential factor is temperature-dependent.
33	The exchange of extracellular GLU is dependent on the forward rate of Reaction 8, the production from BIOM, and the consumption for ANTI. A temperature-dependent constant accounts for the reduced contribution when Reaction 8 reverses direction.

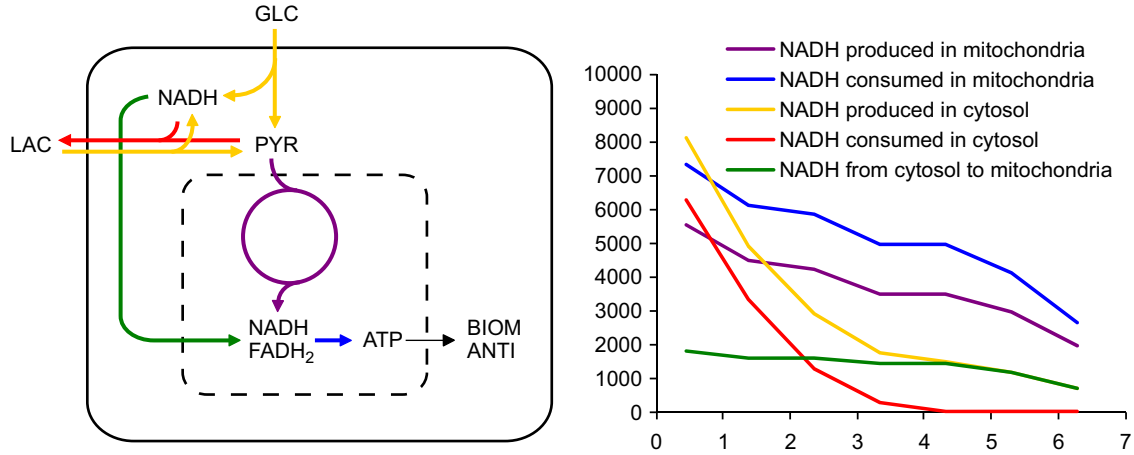


**Fig. 2.** Consumption and production fluxes of NADH in the cytosol and mitochondria based on measured data for a representative CHO fed-batch culture. The x-axis is the culture time in days and the y-axis is the reaction flux in nmol/ $10^6$  cells/day. Note  $FADH_2$  is included in the redox mass balance, but is coupled with NADH for graphical representation.

divided by the rate of NADH transported from the cytosol to the mitochondria.

$$R = \frac{v_{\text{glycolysis} \rightarrow \text{NADH}} + v_{\text{biomass} \rightarrow \text{NADH}}}{v_{\text{NADH} \rightarrow \text{mitochondria}}} = \frac{2v_1 + 0.64v_{16}}{v_{34}} \quad (3)$$

The variable  $R$  accounts for the contribution of NADH to reaction kinetics. When  $R > 1$ , the rate of NADH produced in the cytosol is greater than that transported into the mitochondria. As a result, reactions in the cytosol that use NADH as a cofactor, such as LDH, will proceed in the forward direction at a rate proportional to the magnitude of  $R$ . When  $R = 1$ , it has no effect on the reaction rate. When  $R < 1$ , the demand for NADH in the mitochondria cannot be met by glycolysis and biomass production. To compensate, LDH reverses the direction, with a rate dependent on  $R$ . It should be noted that incorporating the  $R$  variable into the rate expressions significantly influences the simulation results. For example, the  $R$  factor in the equation for LDH sensitizes the entire network to the redox state of the cell. At key time points (e.g. during the temperature shift), even slight changes in the  $R$  value will qualitatively alter the timing and extent of the lactate shift.

## 2.10. Dynamic simulation

**Step 1:** the ‘measured’ reaction rates, i.e. the intracellular reactions which are defined with kinetic rate expressions, are calculated using the extracellular metabolite concentrations,  $R$  value, and parameter values. While the metabolite concentrations and  $R$  value are updated at each iteration, most of the parameter values do not change over the course of a simulation. The only parameters that do change are the rate constants that depend on temperature. **Step 2:** the now calculated ‘measured’ reaction rates are used as inputs for MFA, to calculate the flux distribution for the entire network. **Step 3:** the extracellular metabolite concentrations and  $R$  value are updated from the flux distribution and viable cell density. The  $R$  value is calculated from the equation above. The concentrations are calculated as follows:

$$C_{k,i+1} = C_{k,i} + \frac{v_{k,i}(t_{i+1} - t_i) VCD_i}{1000} \quad (4)$$

where  $C_{k,i+1}$  and  $C_{k,i}$  are the extracellular concentrations of metabolite  $k$  (units of mM) at iterations  $i+1$  and  $i$ , respectively,  $v_{k,i}$  is the exchange flux (units of nmol/ $10^6$  cells/day, and positive for output and negative for input) for metabolite  $k$  at iteration  $i$ ,  $t_{i+1}$  and  $t_i$  are the

time (units of days) at iterations  $i+1$  and  $i$ , respectively, and  $VCD_i$  is the viable cell density (units of  $10^6$  cells/mL) at iteration  $i$ . It should be noted that the metabolite concentrations at iteration  $i+1$  are calculated from the flux distribution and cell density at iteration  $i$ . **Step 4:** after all metabolites are updated, the cell density at iteration  $i+1$  is calculated based on the biomass concentration at iteration  $i+1$  and the viability (defined as a time-dependent function). As long as the time step is small enough, this offset will be negligible. The time step used for the current work was 25% the resolution of the measured data, or 0.25 days. **Step 5:** the time is increased by the time step interval, and if the current time is less than the specified culture duration, the algorithm is repeated for the next iteration.

At each iteration, the program performs two checks. The first check is to see if the current time matches a feed time. If so, the metabolites that are fed are increased by the appropriate concentration. The effect of dilution of the feed medium on all metabolite concentrations is also adjusted. The second check is to see if the current time matches the temperature shift time. If so, the temperature-dependent parameters are adjusted for the new temperature. The time required for a 1 L bioreactor to drop from 37 to 31 °C is on the order of 1 h (data not shown). However, it is assumed based on the measured flux data that the population of cells exhibits a reduction in enzymatic activity more slowly, on the order of 10 h. The reduction in the temperature-dependent parameters is therefore represented by a sigmoidal curve to account for this extended duration.

## 2.11. Parameter estimation

The CHO cell fed-batch model has 47 parameters. The parameter values were estimated by fitting the model to the measured data using the Simulated Annealing toolbox in Matlab. For each potential parameter set, the dynamic simulation ran for 41 iterations (i.e. in culture time, an iteration every 0.25 days from day 0–10). The objective function was to minimize the normalized sum squared difference between the simulated and measured concentrations, summed over all time points and extracellular metabolites

$$\text{Minimize: } \sum_k \sum_t \left( \frac{C_{k,t}^{\text{sim}} - C_{k,t}^{\text{meas}}}{C_{k,t}^{\text{meas}}} \right)^2 \quad \forall k \in \{\text{extracellular metabolites}\} \quad (5)$$

where  $C_{k,t}^{\text{sim}}$  and  $C_{k,t}^{\text{meas}}$  are the simulated and measured concentrations, respectively, of extracellular metabolite  $k$  at time  $t$ . The

**Table 4**  
Kinetic parameter values.

Number	Parameter	Value
1	$v_{\max 1f}$	3800
2	$Ki_1$	20
3	$K_{m1}$	10
4	$exp_{1a}$	3
5	$exp_{1b}$	1
6	$TC_{1b}$	5
7	$v_{\max 2}$	2200
8	$K_{m2}$	6
9	$v_{\max 3f}$	350
10	$v_{\max 3r}$	150
11	$K_{m3a}$	4
12	$K_{m3b}$	2.5
13	$K_{m3c}$	5
14	$TC_{3b}$	5
15	$v_{\max 8f}$	2200
16	$v_{\max 8r}$	200
17	$K_{m8a}$	2.5
18	$K_{m8b}$	1
19	$K_{m8c}$	1
20	$TC_{8b}$	5
21	$v_{\max 9f}$	1
22	$v_{\max 9r}$	1
23	$K_{m9}$	0.7
24	$v_{\max 10f}$	475
25	$v_{\max 10r}$	20
26	$K_{m10a}$	0.3
27	$K_{m10b}$	1
28	$K_{m10c}$	2
29	$TC_{10b}$	1.5
30	$v_{\max 11}$	0.55
31	$v_{\max 12f}$	0.09
32	$v_{\max 12r}$	25
33	$K_{m12a}$	1
34	$K_{m12b}$	3
35	$v_{\max 13}$	30
36	$K_{m13}$	1
37	$v_{\max 16}$	2500
38	$K_{m16a}$	0.4
39	$K_{m16b}$	0.3
40	$K_{m16c}$	20
41	$TC_{16b}$	3
42	$v_{\max 17}$	525
43	$Ki_{17}$	30
44	$exp_{17a}$	0.5
45	$exp_{17b}$	1
46	$v_{\max 33}$	310
47	$K_{m33a}$	4

Units for maximum reaction velocities ( $v_{\max}$ ) are nmol/ $10^6$  cells/day, half-saturation constants ( $K_m$ ) and inhibition constants ( $Ki$ ) are mM, and temperature-dependent constants ( $TC$ ), exponential constants ( $exp$ ), and the redox variable ( $R$ ) are dimensionless.

values of the parameters used for the dynamic simulations are listed in Table 4. It should be noted that a reasonable set of seed parameters was critically important in the regression. Parameter estimation frequently failed to converge when random seeds were used. Therefore, seed parameters were first manually estimated based on experimental data and biochemical knowledge. The parameters were compared to another kinetic model for the human red blood cell (Joshi and Palsson, 1990). The parameters obtained in this study were similar in terms of order of magnitude, i.e.  $K_m$  values were on the order of 1 mM and  $v_{\max}$  values were on the order of 100–1000 nmol/ $10^6$  cells/day.

### 2.12. Sensitivity analysis

For each of the fitted parameters, a span of 19 values was passed into the dynamic simulation. The values tested were 0.1, 0.2, 0.3, 0.4, 0.5, 0.6, 0.7, 0.8, 0.9, 1, 2, 3, 4, 5, 6, 7, 8, 9, and 10 times

the optimal parameter value. The sensitivity of a given parameter  $p$  on a given extracellular metabolite  $k$  was quantified through the variable  $f_{p,k}$ , defined as the normalized summed squared difference between the simulated ( $C_{k,t}^{sim}$ ) and measured ( $C_{k,t}^{meas}$ ) extracellular metabolite concentrations at the same time point  $t$ , summed over all time points

$$f_{p,k} = \sum_t \left( \frac{C_{k,t}^{sim} - C_{k,t}^{meas}}{C_{k,t}^{meas}} \right)^2 \quad \forall k \in \{\text{extracellular metabolites}\} \quad (6)$$

For a given metabolite  $k$ , a  $47 \times 19$  matrix  $F_k$  of  $f$  values was generated with rows for each parameter and columns for each scale factor. For example,  $F_k(1,5)$  represents the normalized summed squared difference between the simulated and measured lactate (extracellular metabolite 4) concentrations over time, when the parameter  $v_{\max 1f}$  (parameter 1) is scaled by 0.5X (parameter scale factor entry 5) the optimal value. The  $f$  values in each row were then normalized by dividing the row by the 1X scale factor  $f$  value for that row. The results for selecting representative  $F_k$  matrices are depicted in Fig. 5, where a colormap represents the extent to which the  $f$  values varied from the optimal.

## 3. Results

### 3.1. Metabolic flux analysis

We first evaluated the quality of the CHO stoichiometric model (Fig. 1) by comparing the experimentally measured and MFA calculated exchange fluxes for external metabolites. Across the different metabolites, the average deviations between the measured and calculated fluxes ranged 0–28%, with 10 of the 13 fluxes less than 10%. Across the different time points, the average deviations were similarly small, ranging 2–19%, with 8 of the 10 time points less than 10%. Furthermore, residuals (defined as the fraction of the sum total exchange flux over the sum positive exchange flux) from elemental balances at 37 and 31 °C were calculated to be 0.8% and 1.1%, respectively, for carbon, and 4.2% and 4.3%, respectively, for nitrogen, averaged over days 0–3 for 37 °C and days 4–10 for 31 °C. These results suggested that the stoichiometric model accurately represented the quantitatively significant pathways in the CHO cell.

The use of MFA assumes that the pseudo-steady state assumption is valid throughout the fed-batch. While the pseudo-steady state assumption is generally invoked for exponential growth, experimental data for multiple cell lines (not shown) revealed that 20 out of the 24 intracellular metabolite concentrations remained constant throughout the fed-batch (i.e. at steady state) and the remaining four metabolite pools changed at rates much less (i.e. three orders of magnitude) than the flux through the respective pools, thereby supporting the use of the pseudo-steady state assumption for all time points (Stephanopoulos et al., 1998).

### 3.2. Simulation accuracy

The model simulated profiles of the extracellular metabolite concentrations and reaction fluxes are shown in Figs. 3 and 4, respectively. The simulations were performed with an initial set of metabolite concentrations and parameter values as the only inputs. The simulated profiles closely tracked the measured profiles. For 9 of 14 metabolites, the fractional deviation of the simulated concentration was less than 50% for all time points; for 12 of the 14 metabolites, the average deviation was less than 30%. Importantly, the simulations correctly predicted both the timing



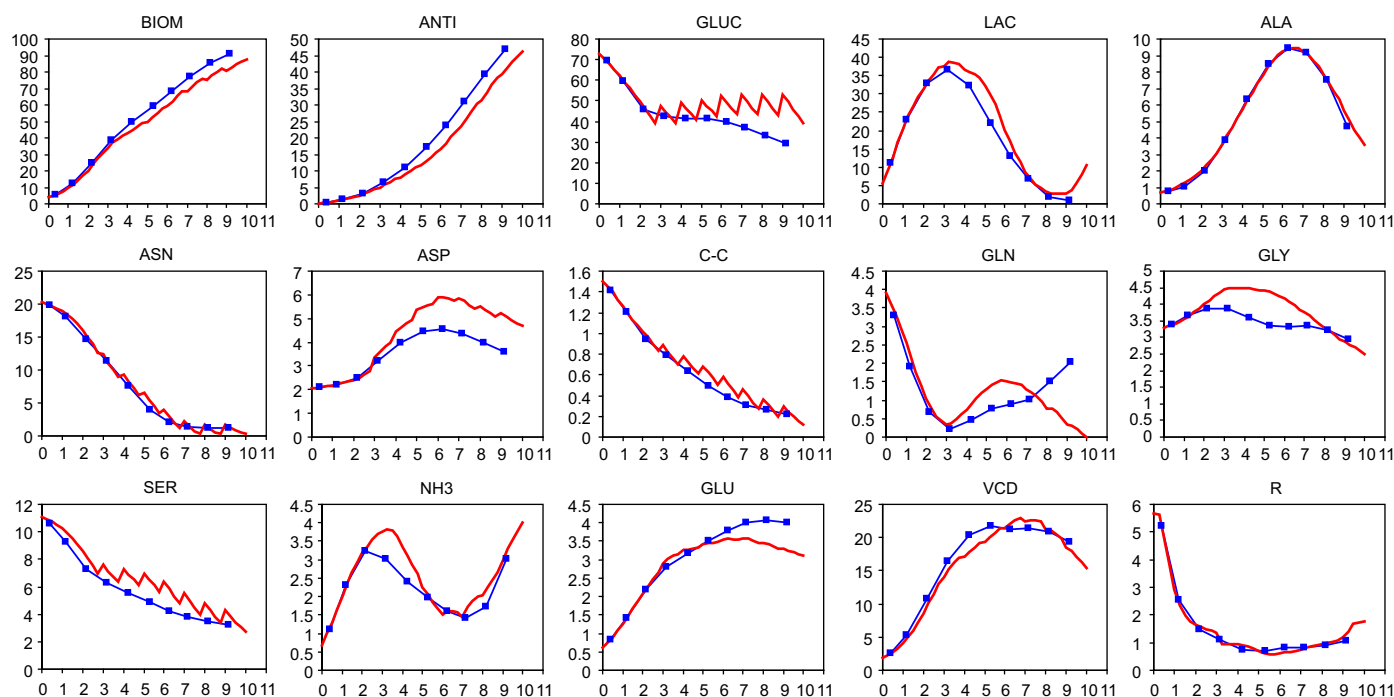


**Fig. 3.** Comparison of measured (blue) and simulated (red) extracellular metabolite concentrations. The x-axis is the culture time in days and the y-axis is concentration in mM, except for viable cell density (VCD) which is  $10^6$  cells/mL and  $R$  which is dimensionless. (For interpretation of the references to colour in this figure legend, the reader is referred to the web version of this article.)

and magnitude of metabolic shifts, which are characterized by transitions from production to consumption of external metabolites, such as lactate and ammonia.

In Fig. 4, the periodicity of many reaction flux profiles observed after day 6 is a result of the biomass flux, which depends on asparagine, whose medium concentration fluctuates significantly with daily feeds. In Fig. 3, the difference ( $>100\%$  after day 4) between the simulated and measured glutamine concentration reflects the sensitivity of this quantity to the net flux of reactions producing and consuming glutamine (i.e. the exchange flux), which fluctuates about 0. Similarly, the discrepancy in the glucose concentration (Fig. 3) can be attributed to the slight deviation between the simulated and measured extracellular lactate concentration, which is sensitive to the redox variable  $R$ .

### 3.3. Model sensitivity

The sensitivity of the model to the fitted parameter values is shown in Fig. 5. Sensitivities were calculated for each metabolite concentration profile as deviations relative to the profile obtained with the *optimal* parameter values. Biomass, antibody, and glucose profiles were largely insensitive to changes in the parameter values, the sum squared errors deviating less than 1000% for 29 out of the 47 parameters tested over a range of 10-fold increase and decrease. This analysis compares the *total* sum squared error between the simulated and measured profiles over *all* 10 time points; when this error is normalized to the error from the optimal profile, the resulting numerical value can be large. However, examination of the corresponding metabolite profiles reveals that the fit is quite accurate even when the deviation is numerically large (see Fig. 6). Alanine, ammonia, and lactate profiles showed greater sensitivities. Each of these metabolites transitioned between net uptake and output at varying points in the fed-batch culture. Not surprisingly, lactate exhibited the largest sensitivity. The lactate flux directly depends on the regulatory variable  $R$ , which in turn is affected by multiple

reactions in different parts of the metabolic network. Even small variations in most pathways can prevent  $R$  from decreasing below unity, leading to a delay or outright absence of a lactate shift.

### 3.4. Model validation

To validate the model, simulated concentration profiles of selected metabolites for representative process conditions were compared with experimentally determined trends (Fig. 7). Fig. 7, row a, shows that the increase in viable cell density from delaying the temperature shift from day 3 to 4 was indeed negated by the concurrent lactate increase and its inhibitory effect, such that the final antibody titer was essentially the same as a temperature shift on day 3. Seeding the reactor at a higher cell density increased the integrated cell density, accelerated the lactate shift, and improved the antibody titer, as predicted by the model simulations (Fig. 7, row b). Fig. 7, row c describes the observed profiles for a non-transfected CHO-K1 cell line in different culture media, which are in good agreement with the simulations. The model correctly predicted that a low productivity cell line grown in a rich medium will not experience a sufficiently large demand on the cytosolic NADH pool to reverse the lactate flux. The predicted response to high basal glutamine was also supported by experiments (Fig. 7, row d). Glutamine had a positive effect on the total integrated cell density, and thus would appear to also increase the final antibody titer. This naïve prediction was neither borne out by the experiments nor by the model simulations, which correctly identified increased lactate production and its negative effect on the productivity.

### 3.5. Process perturbations

Fig. 8 shows the simulated concentration profiles of selected metabolites for representative process conditions. We examined the effects of temperature shift day, seed density, specific productivity, and metabolite concentrations on viable cell

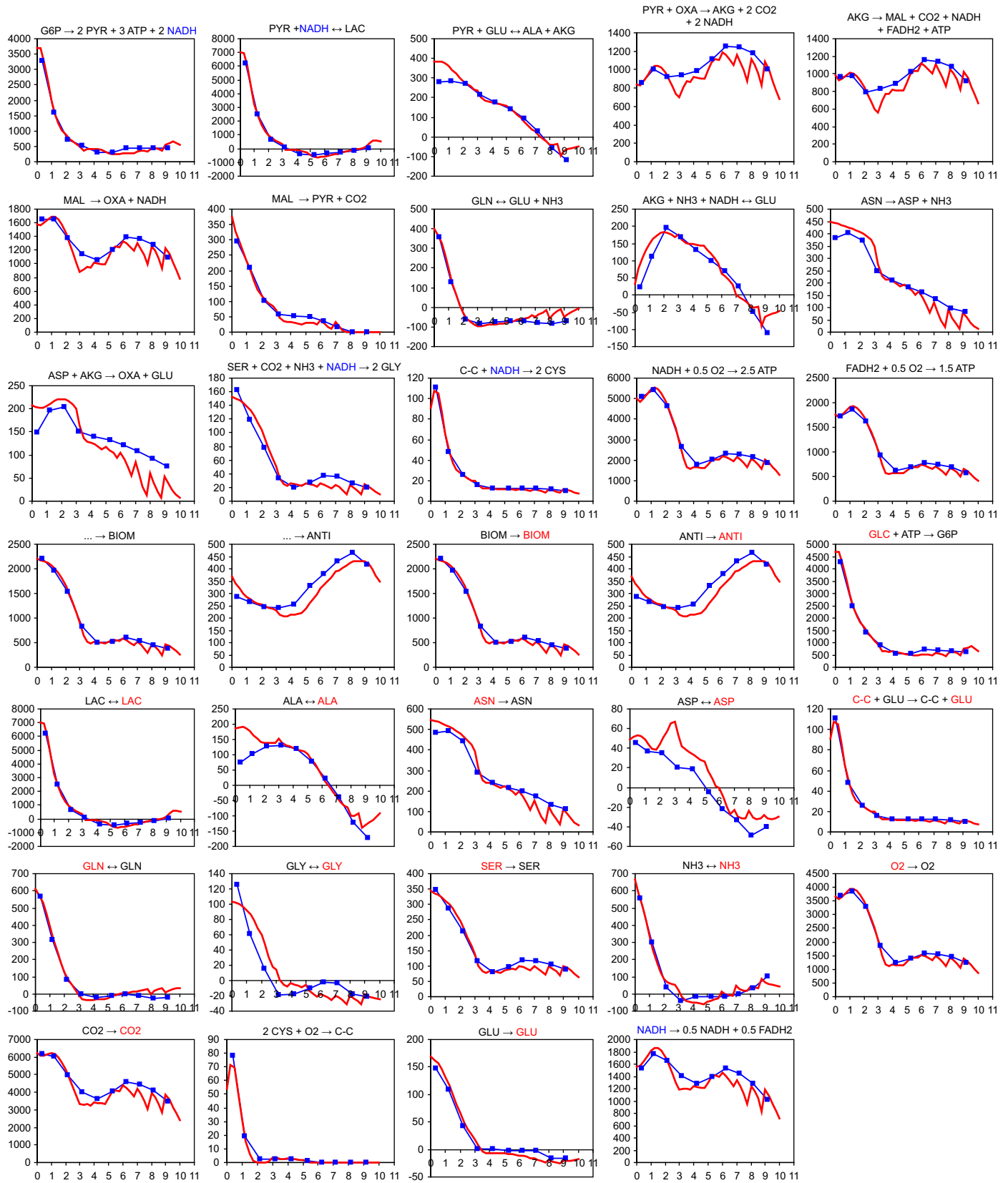


**Fig. 4.** Comparison of MFA calculated (blue) and dynamically simulated (red) reaction fluxes. The x-axis is the culture time in days and the y-axis is the reaction flux in nmol/ $10^6$  cells/day. Metabolites are distinguished by extracellular (red) and intracellular (black). NADH is distinguished by cytosolic (blue) and mitochondrial (black). (For interpretation of the references to color in this figure legend, the reader is referred to the web version of this article.)

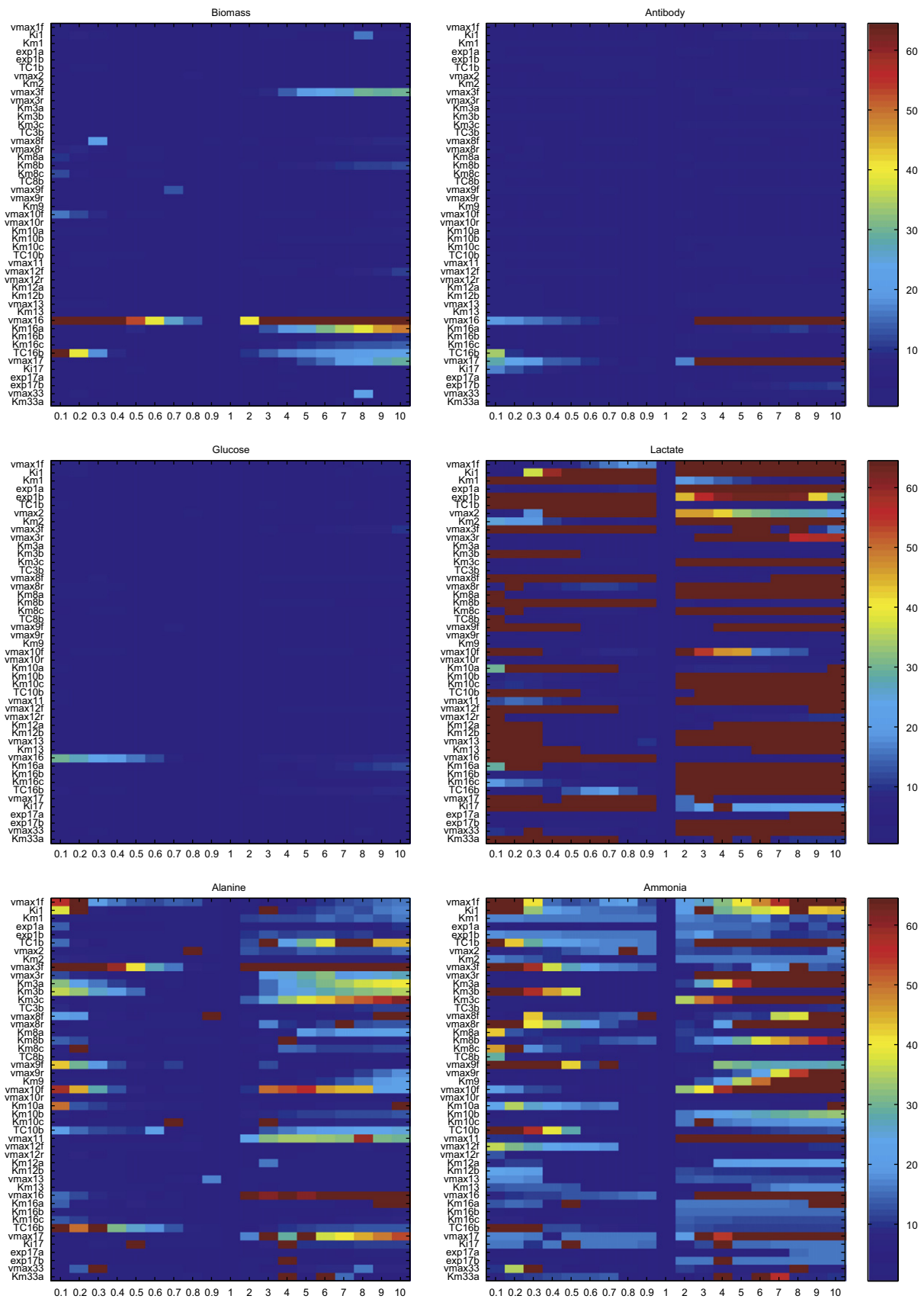


**Fig. 5.** Sensitivity of parameters used in kinetic rate expressions. Each colormap represents the normalized summed squared difference between the simulated and measured extracellular metabolite concentration over time, when the parameter (row) is scaled by a factor (column) of the optimal value. The values for each parameter (row) are normalized by the optimal 1X (middle column) value for that parameter (row). Colors represent the value of the entry in the  $F$  matrix, after row normalization.

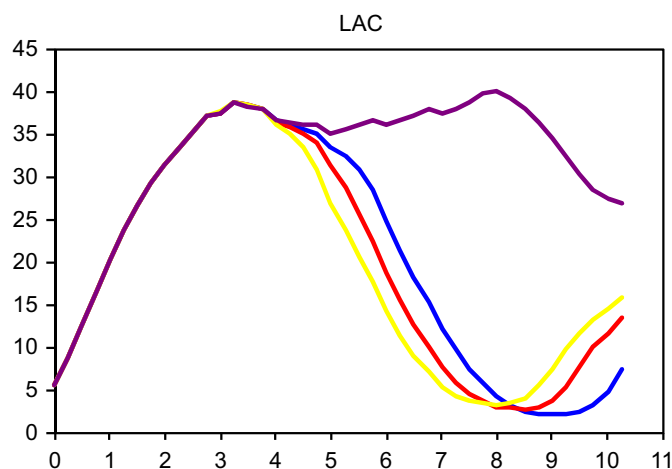


**Fig. 6.** Example of how the percent deviation calculated from the parameter sensitivity analysis corresponds to an actual goodness of fit. The x-axis is the culture time in days and the y-axis is the concentration in mM. Curves correspond to simulations for different scale-factors of the parameter  $K_{m10b}$  that cover a range of percent deviations. The percent deviation is defined as the ratio of the sum squared error, using a given parameter to the sum squared error using the optimal parameter. Here, the sum squared error refers to differences between the simulated and measured lactate concentrations across all time points. The colors correspond to the following: blue: scale-factor=1 (optimal) and deviation=N/A, red: scale-factor=0.7 and deviation=765%, yellow: scale-factor=0.3 and deviation=3096%, purple: scale-factor=2 and deviation=52,326%. (For interpretation of the references to color in this figure legend, the reader is referred to the web version of this article.)

density (VCD), antibody, lactate, asparagine, and the redox variable,  $R$ . The basal condition was specified by the following settings:  $1.8 \times 10^6$  cells/mL seed density, day 3 temperature shift, and a daily feed of 3% v/v starting on day 3.

### 3.5.1. Temperature shift

Fig. 8, row a shows the effect of the timing of the temperature shift. If the temperature shift occurs too early, such as on day 2 (red curve), the lactate concentration will monotonically increase. With a lower viable cell density, the demand for NADH is less than the supply. The  $R$  value, i.e. ratio of NADH production in the cytosol to consumption in the mitochondria, is maintained above unity without a redox adjustment through lactate consumption. If the temperature shift is delayed to day 4 (yellow), the viable cell density increases along with the lactate concentration. The final antibody concentration is not significantly improved compared to a temperature shift on day 3 (blue). If the temperature shift is delayed even further to day 5 (purple), secondary process perturbations occur, for example faster consumption and an eventual depletion of asparagine. Model simulations suggest that supplying extra asparagine in the feed (green) will improve the viable cell density and antibody titer. The simulation results illustrate the wide range of process perturbations that ultimately affect the viable cell density and antibody titer. The weak correlation between viable cell density and antibody production has also been observed experimentally in a number of different settings (Fig. 7).

### 3.5.2. Seed density

Fig. 8, row b illustrates the effect of variations in the seed density. These examples show how at higher seed densities, the rate of nutrient consumption/depletion outside the cell is higher, resulting in compensation from inside the cell to meet the demand, and thereby disrupting the energy balance. The effects of lower seeding density (red) are similar to the early temperature shift (row a, red), decreasing the viable cell density and

suppressing the lactate shift. A culture with low seed density can be forced to exhibit the lactate shift by manipulating the supply of NADH through a reduction in basal glucose and daily media feed (purple). With a reduced supply of NADH from the cytosol,  $R$  drops below one, leading to a net lactate consumption and an increase in antibody titer. Increasing the seeding density (yellow) significantly elevates the antibody concentration. The higher initial viable cell density increases the biomass and antibody concentrations earlier in the culture, leading to a greater ATP and mitochondrial NADH demand. The higher demand for reducing equivalents rapidly lowers the  $R$  value even before the temperature shift. Consequently, the culture is already 'primed' to shift when the temperature is reduced on day 3. With higher viable cell densities, the lactate is consumed quickly, reducing the inhibition on antibody production. On the other hand, the higher viable cell density rapidly depletes the nutrients in the culture medium. Nutrient depletion can be addressed through additional feeds suggested by the model simulation. For example, an extra 2% daily feed (green) improves both the viable cell density and antibody concentration.

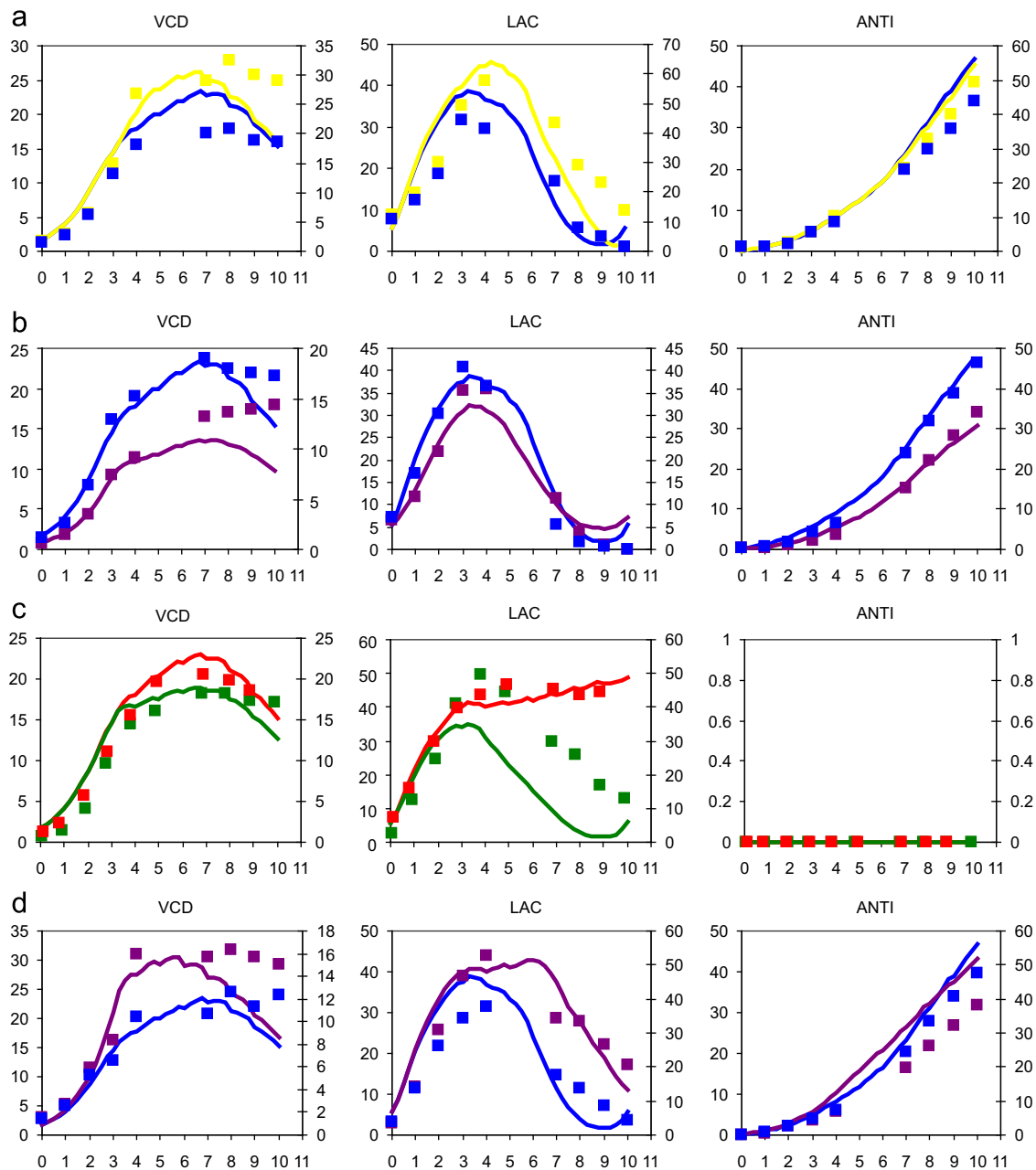
### 3.5.3. Specific productivity

Fig. 8, row c shows the effects of varying the specific productivity, for example, through genetic manipulation. When the productivity ( $v_{max}$  of the antibody reaction) is reduced to 50% (red), the effects are similar to lowering the seeding density (row b, red). Lower antibody production reduces the demand for ATP and mitochondrial NADH such that there is an excess of NADH supply in the cytosol. As a result,  $R$  remains above one and the net lactate consumption does not occur. Simulation results at different antibody productivity levels indicated that there is a minimal threshold associated with the metabolic shift, as decreases in productivity by 50% and 25% (yellow) exhibit nearly identical metabolic profiles. A process with a lower specific productivity can be induced to undergo the metabolic shift by reducing the supply of reducing equivalents. At 50% productivity, lowering the basal glucose and daily feed percentage (green) produces the lactate shift and leads to a higher final antibody concentration (compared to red), despite a lower overall viable cell density. At 200% productivity (purple), the metabolic profile is similar to high seed density (row b, yellow), with an earlier occurrence of the metabolic shift.

### 3.5.4. Nutrient concentrations

Fig. 8, row d illustrates the effect of variations in metabolite concentrations in the basal medium. Lowering the basal glucose concentration (red) reduces the amount of NADH produced in the cytosol, and decreases the  $R$  value below one before the temperature shift, leading to a net consumption of lactate. With diminished inhibition by medium lactate, the antibody productivity is higher (red, days 5–7). However, as the medium lactate level is reduced, the  $R$  value recovers to one. Lactate is produced when  $R$  swings above one, reducing the antibody productivity (red, days 7–10). Starting the culture with low basal glucose and feeding daily from day 1 (yellow) delays the depletion and upswing of lactate (compared to red). However, the initial lactate production is higher, resulting in an antibody productivity that is lower initially and higher later, thus yielding the same (similar) final titer. These examples demonstrate the delicate balance within the cytosol with respect to the redox state and its global impact on metabolic and biosynthetic activities.

The effect of increasing other biomass substrates was also examined. Increasing basal asparagine alone has no effect (data not shown), likely because the control concentration is already



**Fig. 7.** Experimental validation of select simulation conditions. Simulated data is represented with solid lines with corresponding units on the left axis, and experimental data is represented with square symbols with corresponding units on the right axis. Axes labels are the same as Fig. 3. Row “a” depicts data from cultures with temperature shifts on day 3 (blue) or day 4 (yellow). Row “b” depicts data for cultures seeded at low (purple) and high (blue) cell densities. Row “c” depicts data for a non-transfected CHO-K1 cell line that was cultured in enriched (red) or dilute media (green). Row “d” depicts data from cultures grown in control (blue) or increased (purple) levels of basal glutamine. Note that these examples reflect cell lines cultivated with process parameters that were slightly different from those used for deriving the rate expressions and fitting the parameters. However, pH, temperature, and dissolved oxygen (as described in Section 2.1) were identical. Experiments were not performed in replicate, as previous experiments (data not shown) demonstrated a negligible variability (less than 4% difference between replicate cultures in an antibody titer, cell density, and metabolite concentrations), which is typical of well-controlled fed-batch processes (Fan et al., 2009; Sauer et al., 2000). (For interpretation of the references to colour in this figure legend, the reader is referred to the web version of this article.)

above the enzyme saturation levels. Increasing basal glutamine alone (purple) has a significant effect on improving the viable cell density. However, the lactate concentration remained at its peak level for a longer period of time, thereby diminishing the potential benefits of increased antibody concentration. Under control (basal) conditions, the glutamine pool at the time of the temperature shift is nearly depleted, resulting in a draw from the glutamate pool to compensate. Glutamate dehydrogenase, which supplies some of glutamate, requires NADH as a cofactor. When glutamine supply is

abundant, the flux through glutamate dehydrogenase is reduced along with the demand for NADH. Consequently,  $R$  remains steady about one and lactate levels off. When the asparagine pool reaches near depletion (purple, day 6), the supply of glutamate is reduced (via aspartate aminotransferase), and the glutamate dehydrogenase flux increases to the point that the demand for NADH in the mitochondria requires additional supply from the cytosol. At this point,  $R$  drops below one and lactate is consumed. This chain of events is consistent with the simulation, where both glutamine and



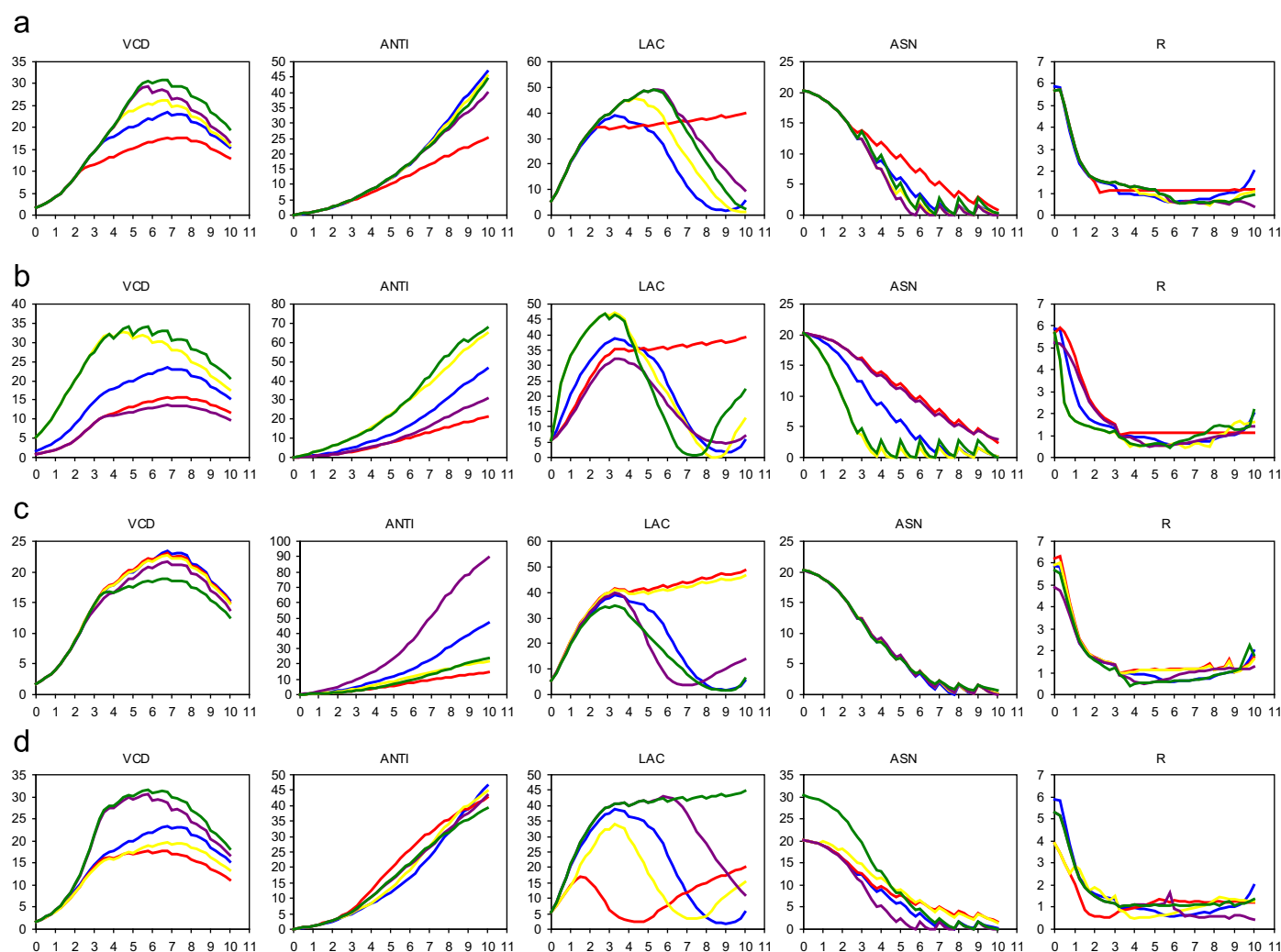


**Fig. 8.** Simulated results using the dynamic model. Axes labels are the same as Fig. 3. The control condition (blue) is the same in each row. Row “a” depicts the effect of the temperature shift day with colors corresponding to the following: blue: day 3 shift, red: day 2 shift, yellow: day 4 shift, purple: day 5 shift, green: day 5 shift with extra asparagine in the feed medium. Row “b” depicts the effect of seed density with colors corresponding to the following: blue:  $1.8 \times 10^6$  cells/mL seed, red:  $0.9 \times 10^6$  cells/mL seed, yellow:  $5.4 \times 10^6$  cells/mL seed, purple:  $0.9 \times 10^6$  cells/mL seed with  $0.5 \times$  basal glucose and 1% less daily feed, green:  $5.4 \times 10^6$  cells/mL with 2% more daily feed. Row “c” depicts the effect of specific productivity with colors corresponding to the following: blue:  $1 \times v_{\max}$  antibody, red:  $0.5 \times v_{\max}$  antibody, yellow:  $0.75 \times v_{\max}$  antibody, purple:  $2 \times v_{\max}$  antibody, green:  $0.5 \times v_{\max}$  antibody with  $0.5 \times$  basal glucose and 1% less daily feed. Row “d” depicts the effect of metabolite concentration with colors corresponding to the following: blue:  $1 \times$  concentrations, red:  $0.16 \times$  basal glucose, yellow:  $0.16 \times$  basal glucose with daily feed starting on day 1, purple: extra basal glutamine, green: extra basal glutamine and asparagine. (For interpretation of the references to colour in this figure legend, the reader is referred to the web version of this article.)

asparagine are increased (green). When both metabolites remain elevated, the drain on glutamate never occurs, and  $R$  remains around one.

#### 4. Discussion

In this paper, we describe the formulation of a kinetic model of CHO cell metabolism for dynamic simulation of metabolic and biosynthetic pathways in the fed-batch culture. The model explicitly accounts for redox- and temperature-dependent changes to pathway activities, and directly calculates the measured variables, i.e. metabolite concentration time profiles in the reactor, by defining rate expressions based on extracellular metabolites. The model simulations successfully predicted the effects of several process perturbations on cell growth and product titer. The simulation results suggest that the metabolic shift of CHO cell fed-batch cultures could involve a redox-dependent mechanism, where the shift is triggered by a deficit

in the supply of reducing cofactors from the cytosol to the mitochondria.

Previous CHO cell models have attempted to simulate fed-batch dynamics based on empirically derived expressions for macroscopic balances, often using different sets of parameters for distinct phases of the culture (Gao et al., 2007; Provost et al., 2006; Xing et al.). In the present model, reactions were represented with rate expressions grounded in enzyme kinetics. Specifically, convenience kinetics was employed, which is a generalized form of Michaelis–Menten type (saturation) kinetics that can be derived from a rapid equilibrium, random-order enzyme mechanism. The advantages of this form are that it accommodates various reaction stoichiometries, describes enzyme regulation by activators and inhibitors, and can be specified by a small number of thermodynamically independent parameters (Liebermeister and Klipp, 2006). To enable direct calculation of measured quantities, we expressed the reaction rates in terms of extracellular, rather than intracellular metabolites. In formulating the rate expressions, especial care was taken to identify the dominant extracellular metabolites that

influence the concentrations of their intracellular counterparts, and thereby preserve the substrate dependences of reactions. For example, for the reaction catalyzed by alanine transaminase, the contribution of pyruvate was accounted for through its precursor metabolites, glucose and lactate. In addition to the substrate variables, the model incorporated a redox state-dependent regulatory variable (i.e.  $R$ ), which enabled simulations of long-term culture dynamics without using separate sets of equations or parameters for each distinct phase (e.g. exponential growth, stationary, and death) of the fed-batch culture.

Surprisingly, basic parameters such as  $v_{\max}$  and  $K_m$  values for a complete CHO metabolic network were not readily available in the published literature. Because the expressions used in previously reported models (Gao et al., 2007; Provost et al., 2006; Xing et al.) are based on macroscopic reactions and Monod growth kinetics, it is difficult to directly compare the parameters from these models to those obtained in the present work. Therefore, the  $v_{\max}$  parameters of the present study were compared to metabolic flux data, assuming that the steady state flux of a reaction during balanced growth reflects the corresponding enzyme's activity near saturation. The  $v_{\max}$  of glucose uptake ( $v_{\max1f}$ ) was calculated as 3800 nmol/10<sup>6</sup> cells/day, which is in good agreement with previously reported, representative flux values of 1700 (Altamirano et al., 2001) and 3250 nmol/10<sup>6</sup> cells/day (Nyberg et al., 1999). Similar agreement was found for other  $v_{\max}$  parameters. The  $v_{\max}$  of lactate dehydrogenase ( $v_{\max2}$ ) was calculated as 2200 nmol/10<sup>6</sup> cells/day and reported as 2250 (Altamirano et al., 2001) and 3670 nmol/10<sup>6</sup> cells/day (Nyberg et al., 1999). The  $v_{\max}$  of alanine transaminase ( $v_{\max3f}$ ) calculated as 350 nmol/10<sup>6</sup> cells/day and reported as 183 (Altamirano et al., 2001) and 225 nmol/10<sup>6</sup> cells/day (Nyberg et al., 1999). The  $v_{\max}$  of glutaminase ( $v_{\max8f}$ ) calculated as 2200 nmol/10<sup>6</sup> cells/day and reported as 1820 nmol/10<sup>6</sup> cells/day (Nyberg et al., 1999). The broad agreement between reported flux data and the  $v_{\max}$  values suggests that the parameter values used in this study are not just empirically obtained fits, but are also physiologically meaningful.

Unlike the parameters, the structure of the model equations is generic with respect to the type of mammalian cell and recombinant protein, i.e. specificity for the CHO cell and fed-batch process results from the parameters. In principle, application of the model to other parental CHO or mammalian cell lines, different culture processes, or extreme operating conditions would likely require re-estimation of at least some of the parameters. The simulations in Fig. 7 show that the time profiles calculated with a given parameter set derived from one cell line/process condition differs in magnitude from the profiles measured for another cell line/process condition. However, if the goal is to predict the responses to a culture perturbation relative to a control cell line/process condition, such re-estimation may not be necessary. For example, in the same Fig. 7, the simulated trends achieve not only qualitative accuracy in terms of the direction of the responses, but also the relative magnitude of the changes, even though the simulation parameters were defined for a different parental cell line than the measured data.

One of the major achievements of the model presented herein is the ability to accurately predict the timing and magnitude of the metabolic shift. To the best of our knowledge, these predictions have not been achieved in the previous works. Our simulations (Fig. 8) suggest that the metabolic shift reflects a disruption in the balance between cytosolic supply and mitochondrial demand for reducing equivalents. Specifically, a shortage in the supply of NADH reverses the net flux of redox reactions such as LDH, which would add to the supply of reducing equivalents in the cytosol, and rebalance the cytosolic and mitochondrial redox fluxes. In this regard, the metabolic shift could result from a set of concerted, compensatory actions that

involve multiple redox sensitive pathways. Our model captures these actions by incorporating the redox flux ratio  $R$  into the reaction rate expressions. Implicit in the use of the variable  $R$  is the assumption that balancing the mitochondrial demand for reducing equivalents is a dominant metabolic objective of the CHO cell. We found that this was a reasonable assumption, as previous studies in cancer metabolism have demonstrated regulatory mechanisms that act to maintain redox homeostasis under perturbed (hypoxic) conditions, thereby prolonging cell survival (Semenza, 2009).

One potential drawback of the model is the reliance on flux balances. The assumption of pseudo-steady state, while supported experimentally, is still only an approximation, which ultimately prevents detailed calculations of dynamic changes within the cell. For example, the present model does not account for fluctuations in intracellular metabolite concentrations that are not reflected in the extracellular environment. Consequently, molecular mechanisms of pathway regulation, involving the accumulation or dissipation of signaling metabolites, cannot be directly explained or tested. In the present study, we found that this loss of detail did not compromise the ability of the model to simulate the long-term dynamics of a fed-batch culture. Prospectively, additional details of molecular regulation could be implemented by building layers into the model. For example, an integrated FBA (iFBA) (Covert et al., 2008) uses rate law-derived ordinary differential equations (ODEs) to trace the dynamics of a subset of metabolites in the metabolic network over short time scales. The rates calculated by the ODEs are then used to update the flux equality constraints for an FBA of the entire network. The iFBA framework could be adopted for the present model such that the mechanism-based governing equations may be written around key regulatory metabolites, which could then be incorporated as additional variables into the reaction rate expressions.

Second, the model omits some significant metabolic and process regulators. For example, the present model did not include reactions involving glutathione, which acts as a major redox buffer by scavenging reactive oxygen species (Schafer and Buettner, 2001). Including reactions that describe the intracellular cycling of glutathione, while challenging, would not only provide additional constraints for related metabolites such as cysteine and glutamate, but also more thoroughly account for the metabolism of reducing equivalents, especially NADPH. Regeneration of reduced glutathione (GSH) from its oxidized form (GSSG) via glutathione reductase directly depends on the availability of NADPH. Process regulators pH and osmolarity were also neglected, both of which have been shown, at least empirically, to influence central metabolism and antibody synthesis (Ozturk and Palsson, 1991; Reddy and Miller, 1994). In fact, omission of these variables is likely a contributing factor to the discrepancies observed between the predicted and simulated antibody profiles for some conditions in Fig. 7. As there are a number of options to control the pH and osmolarity of a fed-batch culture, including these variables in a predictive simulation model would be clearly valuable for process optimization. However, due to the multiple mechanistic roles of these variables (Oh et al., 1995; Osman et al., 2001), it is difficult to incorporate them into rate expressions without some empiricism. One approach is to incorporate these variables into kinetic rate expressions as  $v_{\max}$  scale-factors (Vinnakota et al., 2006). At the present time, this empirical approach would require a very large experimental effort, because the scaling factors would need to be estimated from experimental data for each enzyme at multiple different states. In this regard, one possible next step in refining the model would be to first focus on the direct dependencies of the antibody titer on cell viability, pH, osmolarity, and other process variables. This refinement would require additional culture data

that describe significant variations in the antibody titer with changes in the aforementioned variables.

Third, the model currently lacks the ability to predict changes in cell viability and antibody product quality (i.e. glycosylation, under disulfide bond formation, and high molecular weight species). It is envisioned that in future model versions, viability could be incorporated through an additional model level that includes cell cycle dynamics or as a function of cell age dependent metabolic changes (Chrysanthopoulos et al., 2010). Aspects of product quality could be predicted from representative cellular metabolic markers, such as the redox variable (Trexler-Schmidt et al., 2010).

Finally, some results from the model simulations are inconsistent, in an absolute sense, with previously reported values. In particular, the MFA results from the current model predict a respiratory quotient (RQ) ranging 1.5–2.8 over the duration of the fed-batch. These values are outside the range of values typically reported for CHO cell metabolism (Altamirano et al., 2001; Gray et al., 1996), which are around 1. On the other hand, the carbon and nitrogen balances closed completely or nearly completely over all time points, suggesting that the model accounted for all major pathways with reasonable accuracy. Moreover while the RQ was outside the expected range, the OURs and carbon evolution rates (CERs) were comparable to previously reported values. The OUR values measured in the present study (e.g. 3300 nmol/10<sup>6</sup> cells/day on day 2) are of the same order magnitude, but somewhat lower than values reported in other studies (e.g. 3600 (Deshpande and Heinzle, 2004) to 4800 (Ducommun et al., 2000) nmol/10<sup>6</sup> cells/day for equivalent day 2 cultures). The CER is on the upper end of previously reported values (e.g. 5000 nmol/10<sup>6</sup> cells/day on day 2, compared to the same reported OUR range).

Despite the aforementioned limitations, the dynamic model described herein generated simulations that accurately described the metabolic shift and other dynamic features of long-term, high-density fed-batch culture of CHO cells. Further work is warranted to extend the model to more broadly capture the variables affecting the antibody profile. Prospectively, the extended model could be used to not only optimize the process parameters, but also to gain additional insight into the dynamics of dependencies between CHO cell metabolism and antibody synthesis.

## Acknowledgments

The authors gratefully acknowledge support by Pfizer (formerly Wyeth BioPharma), Tufts University, and NSF (Award no. 0829899).

## References

- Altamirano, C., Illanes, A., Casablanco, A., Gamez, X., Cairo, J.J., Godia, C., 2001. Analysis of CHO cells metabolic redistribution in a glutamate-based defined medium in continuous culture. *Biotechnol. Prog.* 17, 1032–1041.
- Boghigian, B.A., Seth, G., Kiss, R., Pfeifer, B.A., 2010. Metabolic flux analysis and pharmaceutical production. *Metab. Eng.* 12, 81–95.
- Bonarius, H.P., Hatzimanikatis, V., Meesters, K.P., de Gooijer, C.D., Schmid, G., Tramper, J., 1996. Metabolic flux analysis of hybridoma cells in different culture media using mass balances. *Biotechnol. Bioeng.* 50, 299–318.
- Butler, M., 2005. Animal cell cultures: recent achievements and perspectives in the production of biopharmaceuticals. *Appl. Microbiol. Biotechnol.* 68, 283–291.
- Chassagnole, C., Noisommit-Rizzi, N., Schmid, J.W., Mauch, K., Reuss, M., 2002. Dynamic modeling of the central carbon metabolism of *Escherichia coli*. *Biotechnol. Bioeng.* 79, 53–73.
- Chrysanthopoulos, P.K., Goudar, C.T., Klapa, M.I., 2010. Metabolomics for high-resolution monitoring of the cellular physiological state in cell culture engineering. *Metab. Eng.* 12, 212–222.
- Covert, M.W., Xiao, N., Chen, T.J., Karr, J.R., 2008. Integrating metabolic, transcriptional regulatory and signal transduction models in *Escherichia coli*. *Bioinformatics* 24, 2044–2050.
- Deshpande, R.R., Heinzle, E., 2004. On-line oxygen uptake rate and culture viability measurement of animal cell culture using microplates with integrated oxygen sensors. *Biotechnol. Lett.* 26, 763–767.
- Ducommun, P., Ruffieux, P., Furter, M., Marison, I., von Stockar, U., 2000. A new method for on-line measurement of the volumetric oxygen uptake rate in membrane aerated animal cell cultures. *J. Biotechnol.* 78, 139–147.
- Fan, L., Zhao, L., Sun, Y., Kou, T., Zhou, Y., Tan, W.S., 2009. A high-yielding, generic fed-batch process for recombinant antibody production of GS-engineered cell lines. *J. Microbiol. Biotechnol.* 19, 1695–1702.
- Gao, J., Gorenflo, V.M., Schärer, J.M., Budman, H.M., 2007. Dynamic metabolic modeling for a MAB bioprocess. *Biotechnol. Prog.* 23, 168–181.
- Goudar, C., Biener, R., Boisart, C., Heidemann, R., Piret, J., de Graaf, A., Konstantinov, K., 2010. Metabolic flux analysis of CHO cells in perfusion culture by metabolite balancing and 2D [<sup>13</sup>C, <sup>1</sup>H] COSY NMR spectroscopy. *Metab. Eng.* 12, 138–149.
- Gray, D.R., Chen, S., Howarth, W., Inlow, D., Maiorella, B.L., 1996. CO<sub>2</sub> in large-scale and high-density CHO cell perfusion culture. *Cytotechnology* 22, 65–78.
- Harris, M., 2009. Market-Leading Biotechnology Drugs 2009: Blockbuster Dynamics in an Ailing Economy. BioWorld, Atlanta, GA.
- Hjersted, J.L., Henson, M.A., 2006. Optimization of fed-batch *Saccharomyces cerevisiae* fermentation using dynamic flux balance models. *Biotechnol. Prog.* 22, 1239–1248.
- Hundal, H.S., Rennie, M.J., Watt, P.W., 1989. Characteristics of acidic, basic and neutral amino acid transport in the perfused rat hindlimb. *J. Physiol.* 408, 93–114.
- Joshi, A., Palsson, B.O., 1990. Metabolic dynamics in the human red cell. Part III—metabolic reaction rates. *J. Theor. Biol.* 142, 41–68.
- Legmann, R., Schreyer, H.B., Combs, R.G., McCormick, E.L., Russo, A.P., Rodgers, S.T., 2009. A predictive high-throughput scale-down model of monoclonal antibody production in CHO cells. *Biotechnol. Bioeng.* 104, 1107–1120.
- Liebermeister, W., Klipp, E., 2006. Bringing metabolic networks to life: convenience rate law and thermodynamic constraints. *Theor. Biol. Med. Modeling.* 3, 41.
- Luan, Y., Wang, W., Nolan, R., Drapeau, D., 2007. Rationally designed media for cell culture. United States Patent Application 20080108553.
- Ma, N., Ellet, J., Okediadi, C., Hermes, P., McCormick, E., Casnocha, S., 2009. A single nutrient feed supports both chemically defined NS0 and CHO fed-batch processes: improved productivity and lactate metabolism. *Biotechnol. Prog.* 25, 1353–1363.
- Mahadevan, R., Edwards, J.S., Doyle 3rd, F.J., 2002. Dynamic flux balance analysis of diauxic growth in *Escherichia coli*. *Biophys. J.* 83, 1331–1340.
- Meadows, A.L., Karnik, R., Lam, H., Forestell, S., Snedecor, B., 2009. Application of dynamic flux balance analysis to an industrial *Escherichia coli* fermentation. *Metab. Eng.*
- Nolan, R., Lee, K., 2009. Modeling the dynamics of cellular networks. In: Jayaraman, A., Hahn, J. (Eds.), *Methods in Bioengineering: Systems Analysis of Biological Networks*. Artech House Publishers.
- Nyberg, G.B., Balcarcel, R.R., Follstad, B.D., Stephanopoulos, G., Wang, D.I., 1999. Metabolic effects on recombinant interferon-gamma glycosylation in continuous culture of Chinese hamster ovary cells. *Biotechnol. Bioeng.* 62, 336–347.
- Oddone, G.M., Mills, D.A., Block, D.E., 2009. A dynamic, genome-scale flux model of *Lactococcus lactis* to increase specific recombinant protein expression. *Metab. Eng.* 11, 367–381.
- Oh, S.K., Chua, F.K., Choo, A.B., 1995. Intracellular responses of productive hybridomas subjected to high osmotic pressure. *Biotechnol. Bioeng.* 46, 525–535.
- Osman, J.J., Birch, J., Varley, J., 2001. The response of GS-NS0 myeloma cells to pH shifts and pH perturbations. *Biotechnol. Bioeng.* 75, 63–73.
- Ozturk, S.S., Palsson, B.O., 1991. Growth, metabolic, and antibody production kinetics of hybridoma cell culture: 2. Effects of serum concentration, dissolved oxygen concentration, and medium pH in a batch reactor. *Biotechnol. Prog.* 7, 481–494.
- Provost, A., Bastin, G., Agathos, S.N., Schneider, Y.J., 2006. Metabolic design of macroscopic bioreaction models: application to Chinese hamster ovary cells. *Bioprocess. Biosyst. Eng.* 29, 349–366.
- Quek, L.E., Dietmair, S., Kromer, J.O., Nielsen, L.K., 2010. Metabolic flux analysis in mammalian cell culture. *Metab. Eng.* 12, 161–171.
- Reddy, S., Miller, W.M., 1994. Effects of abrupt and gradual osmotic stress on antibody production and content in hybridoma cells that differ in production kinetics. *Biotechnol. Prog.* 10, 165–173.
- Sainz, J., Pizarro, F., Perez-Correa, J.R., Agosin, E., 2003. Modeling of yeast metabolism and process dynamics in batch fermentation. *Biotechnol. Bioeng.* 81, 818–828.
- Sato, H., Shiiya, A., Kimata, M., Maehara, K., Tamba, M., Sakakura, Y., Makino, N., Sugiyama, F., Yagami, K., Moriguchi, T., Takahashi, S., Bannai, S., 2005. Redox imbalance in cystine/glutamate transporter-deficient mice. *J. Biol. Chem.* 280, 37423–37429.
- Sauer, P.W., Burky, J.E., Wesson, M.C., Starnard, H.D., Qu, L., 2000. A high-yielding, generic fed-batch cell culture process for production of recombinant antibodies. *Biotechnol. Bioeng.* 67, 585–597.
- Schafer, F.Q., Buettner, G.R., 2001. Redox environment of the cell as viewed through the redox state of the glutathione disulfide/glutathione couple. *Free Radical Biol. Med.* 30, 1191–1212.
- Semenza, G.L., 2009. Regulation of cancer cell metabolism by hypoxia-inducible factor 1. *Semin. Cancer Biol.* 19, 12–16.

- Sheikh, K., Forster, J., Nielsen, L.K., 2005. Modeling hybridoma cell metabolism using a generic genome-scale metabolic model of *Mus musculus*. *Biotechnol. Prog.* 21, 112–121.
- Stephanopoulos, G., Aristidou, A.A., Nielsen, J.H., 1998. *Metabolic Engineering: Principles and Methodologies*. Academic Press, San Diego.
- Trexler-Schmidt, M., Sargis, S., Chiu, J., Sze-Khoo, S., Mun, M., Kao, Y.H., Laird, M.W., 2010. Identification and prevention of antibody disulfide bond reduction during cell culture manufacturing. *Biotechnol. Bioeng.* 106, 452–461.
- Vinnakota, K., Kemp, M.L., Kushmerick, M.J., 2006. Dynamics of muscle glycogenolysis modeled with pH time course computation and pH-dependent reaction equilibria and enzyme kinetics. *Biophys. J.* 91, 1264–1287.
- Xing, Z., Bishop, N., Leister, K., Li, Z.J., 2006. Modeling kinetics of a large-scale fed-batch CHO cell culture by Markov chain Monte Carlo method. *Biotechnol. Prog.* 2, 208–219.
- Zupke, C., Stephanopoulos, G., 1995. Intracellular flux analysis in hybridomas using mass balances and in vitro  $^{13}\text{C}$  nmr. *Biotechnol. Bioeng.* 45, 292–303.